Chemical Engineering Journal 503 (2025) 158272

Contents lists available at ScienceDirect

Chemical Engineering Journal

journal homepage: www.elsevier.com/locate/cej

A comprehensive optimization of highly efficient MA-Free wide-bandgap perovskites for 4-T Perovskite/Silicon tandem solar cells

Yu-Ching Huang [a,b,c,*], Sheng-Wen Huang [a], Chia-Feng Li [d], Shih-Han Huang [b,c], Feng-Yu Tsai [d], Wei-Fang Su [a,d]

[a] Department of Materials Engineering, Ming Chi University of Technology, New Taipei City 24301, Taiwan
[b] Organic Electronics Research Center, Ming Chi University of Technology, New Taipei City 24301, Taiwan
[c] Center for Sustainability and Energy Technologies, Chang Gung University, Taoyuan 33302, Taiwan
[d] Department of Materials Science and Engineering, National Taiwan University, Taipei 10617, Taiwan

ARTICLE INFO

Keywords:
MA-free
Wide-bandgap
Perovskite
Tandem
Lattice strain-induced phase segregation

ABSTRACT

Perovskite/silicon tandem solar cells have emerged as a highly promising strategy for surpassing the Shockley–Queisser limit. Among these tandem solar cells, the wide-bandgap perovskite plays a key role in highly efficient tandem solar cells. However, the wide bandgap perovskite material suffers from considerable voltage loss due to a high trap density and phase instability under light illumination. In this study, we present a comprehensive set of optimization procedures designed to enhance the power conversion efficiency of methylammonium-free (MA-free) wide-bandgap perovskites. Following this procedure, the opaque MA-free wide-bandgap perovskite solar cells demonstrate an impressive efficiency of 22.11 % with a minimal open-circuit voltage deficit of 0.47 V. Moreover, the efficiency of the semi-transparent wide-bandgap perovskite solar cells reached 19.21 %, and these semi-transparent cells were subsequently integrated into a 4-terminal perovskite/Si tandem solar cell, yielding a remarkable efficiency of 29.98 %. Our study paves a facile way towards highly efficient wide-bandgap perovskite solar cells for the application of semi-transparent and tandem solar cells.

1. Introduction

Clean energy has become imperative in achieving the goal of net zero carbon emissions, with solar cells being a key technology for clean energy. In the past few decades, single-junction Si-based solar cells have dominated the solar market. However, due to thermalization and absorption loss, the power conversion efficiency (PCE) of single-junction solar cells cannot surpass the Shockley–Queisser theoretical PCE limit of 33 %.[1] To further boost the PCE, multi-junction tandem solar cells have attracted great attention, capable of pushing the PCE of the two-junction tandem solar cells to 42 %.[2] Based on electrode connections, the architectures of tandem solar cells are primarily categorized into 2-terminal (2T) and 4-terminal (4T) stacking designs. In the 2T structure, the two sub-cells are directly connected in series, necessitating a good interfacial contact and an effective recombination layer between the two sub-cells, which significantly amplifies process complexity. In contrast, the 4T structure involves mechanically stacking the two sub-cells through external circuitry. Although external circuitry adds to the overall cost, it offers the advantage of individually optimizing each sub-cell, thereby simplifying the manufacturing process. In addition, the 4T structure presents a commercial appeal by enabling the replacement of only the faulty sub-cell instead of discarding the entire tandem solar cell, reducing waste and cost.

The two-junction tandem solar cells typically comprise two sub-cells with complementary absorption regions. For Si-based tandem solar cells, a wide-bandgap (WBG) sub-cell is selected to be stacked atop the Si-based solar cells, ensuring the efficient utilization of high-energy photons. Perovskite solar cells (PSCs) emerge as the prime candidate for integration with Si-based solar cells due to the advantages of high PCE, tunable bandgap, low manufacturing cost, mechanical flexibility, and lightweight. Recent research has extensively explored WBG PSCs for various tandem architectures. [3–9] Through simulations, it has been determined that the optimal bandgap for PSCs in perovskite/Si 4T tandem cells falls within the range of 1.6–1.75 eV.[10] Y. Chen et al. successfully adjusted the bandgap of the perovskite layer to 1.63 eV, and achieved the deposition of high-quality perovskite films through seed-

* Corresponding author.
E-mail address: huangyc@mail.mcut.edu.tw (Y.-C. Huang).

https://doi.org/10.1016/j.cej.2024.158272
Received 28 August 2024; Received in revised form 20 November 2024; Accepted 2 December 2024
Available online 3 December 2024

assisted growth. This advancement substantially elevated the PCE of the 4T tandem solar cell to 28.3 %. The highly efficient and stable WBG PSCs significantly contribute to realizing high-PCE perovskite/Si 4T tandem devices. However, it is noteworthy that WBG PSCs grapple with a notable issue of open-circuit voltage (V_{oc}) loss, creating a disparity between their PCE and the ideal PCE. Consequently, the effective reduction of V_{oc} loss emerges as a crucial avenue for enhancing the PCE of WBG PSCs.

Various strategies employed for enhancing the PCE of WBG PSCs, including precursor composition adjustment, addition of solvent additives, and interfacial modification.[11–15] Recent advancements in perovskite compositions have focused on the formamidinium (FA) system, incorporating additional ions like cesium (Cs) and MA to stabilize the α-$FAPbI_3$ crystal phase.[16–19] Considering the potential detrimental impact of MA ion on device stability, the development of an entirely MA-free perovskite is a critical path in advancing PSC technology. Recent studies have been devoted to optimizing the phase stability of MA-free perovskites, revealing that the grain growth control in MA-free perovskites differs significantly from that in MA-containing perovskites.[20–22] Different crystal growth rates in perovskite films induce lattice strain, which may lower the energy barrier for defect formation and promote undesirable phase transitions in perovskite.[23,24] X. Zhuang et al. have identified that the mismatch between Cs and FA in MA-free perovskites affects the film morphology and lattice structure of the films, leading to bandgap shifts. They employed CsCl: Eu^{3+} quantum dots to mitigate the lattice contraction in MA-free perovskite, effectively reducing defect formation and achieve a record PCE of 24.13 % for MA-free PSCs.[25] These studies imply that the lattice structure and strain are the key factors for the PCE enhancement of MA-free PSCs. Therefore, direct extrapolation of results from MA-containing perovskites to MA-free perovskites is deemed inappropriate. This paradigm may hinder the advancement of MA-free perovskites, thus prompting us to conduct a comprehensive reexamination of their characteristics. Liberated from this constraining conceptual framework, our approach has facilitated a breakthrough in the PCE of MA-free wide-bandgap perovskite solar cells.

In addition, WBG PSCs were often contained by a high concentration of bromine (Br) ions, which can trigger photo-generated phase segregation under light illumination. Notably, Cs and MA ions have been shown to effectively mitigate photo-induced phase segregation in WBG perovskite crystals. However, current literature predominantly focuses on light-induced perovskite phase segregation and its impact on device performance, leaving a noticeable gap in comprehensive investigations into crystal-lattice-induced phase segregation of MA-free WBG PSCs. In this work, we uniquely address this limitation by thoroughly elucidating lattice stress accumulation as a significant contributor to phase segregation in MA-free WBG perovskites. This revelation is pivotal in influencing the phase stability and performance of wide-bandgap PSCs. To mitigate the lattice stress effect on phase segregation, the ionic additives with varying ionic radii was introduced to manipulate the distortion of perovskite crystals. Employing rubidium (Rb) cations, we attained high-efficiency, MA-free WBG PSCs with a bandgap of 1.65 eV and PCEs reaching up to 21.95 %. When combined with our previous transparent perovskite solar cell technology, the highest PCE for semi-transparent devices reached 19.21 %, resulting in a 4T Si/PSCs tandem solar cell with a remarkable PCE of 29.98 %. The insights derived from our results provide a comprehensive understanding of the phase stabilization mechanism in perovskites, an imperative aspect for propelling perovskite technology towards the dual goals of heightened efficiency and stability in the future.

2. Results and Discussion

Firstly, to elucidate the correlation between the composition of $Cs_xFA_{1-x}Pb(I_yBr_{1-y})_3$ and the bandgap, we fabricated a series of perovskite films with x ranging from 10 % to 30 % and y ranging from 10 % to 30 %. We control the Cs/FA and Br/I ratios in the composition by adjusting the concentration of CsI/FAI and FABr/FAI in the perovskite precursors, respectively. The determination of bandgaps for various perovskite film compositions was carried out through Tauc plot analysis, with the results presented in Fig. S1. We first derive 2-dimensional quadratic polynomials to more accurately quantify the relationship between MA-free WBG composition and bandgap, as illuminated in Fig. 1a. We chose perovskite compositions with bandgap near 1.65 eV and tolerance factors exceeding 0.9, which are, $Cs_{0.1}FA_{0.9}Pb(I_{0.75}Br_{0.25})_3$ (Cs10Br25), $Cs_{0.2}FA_{0.8}Pb(I_{0.8}Br_{0.2})_3$ (Cs20Br20), $Cs_{0.3}FA_{0.7}Pb(I_{0.85}Br_{0.15})_3$ (Cs30Br15), $Cs_{0.4}FA_{0.6}Pb(I_{0.9}Br_{0.1})_3$ (Cs40Br10) for subsequent discussions. Due to the high Br ratio, the photo-induced phase segregation significantly contributes to V_{oc} loss in the WBG PSCs.[26–28] Fig. S2 is the maximum power point (MPP) tracking of PSCs using different composition. After few seconds, the compositions with higher Br content and lower Cs concentrations are more susceptible to phase separation under illumination at the initial stage. Further, we utilized the photoluminescence (PL) spectra to conduct the phase stability of WBG perovskite films for longer irradiated time of 30 min, as depicted in Fig. 1b. As the Cs ion concentration gradually increased to 30 %, the decreasing blueshift of PL indicates a reduction in photo-induced phase segregation. However, when the Cs ion concentration reached 40 %, the initial PL signal displayed some redshift even before illumination. Due to the small ionic radius of Cs ions, an excessive introduction of Cs ions may lead to phase segregation due to lattice stress, which can be verified by the changes in the UV–vis spectrum of Cs40Br10 (Fig. S3). The PL results revealed an abnormal redshift in the Cs40Br10 device, suggesting that the cause of phase segregation at high Cs ion concentration is different from that at high Br ion concentration. We infer that the phase segregation at high Cs ion concentration is due to excessive lattice stress accumulation.

To comprehend the correlation between Cs ion content and the phase stability of perovskite films, we conducted X-ray diffraction (XRD) analysis of the four perovskite films, as displayed in Fig. 1c. A new peak emerges around a diffraction angle of 23° with the gradual increase of Cs ion concentration, signifying a transformation of the original α-phase perovskite crystal to the β-phase due to the incorporation of Cs ions with a small ionic radius. Upon further raising the Cs ion concentration to 40 % (Cs40Br10), we observed the emergence of an additional δ-phase alongside the β-phase peak. The appearance of the δ-phase is attributed to the substantial lattice stress induced by the high doping of Cs ions and is confirmed by the UV–Vis spectra of the perovskite films, depicted in Fig. S3. The Cs40Br10 film exhibits a second absorption peak around the 450 nm wavelength, identifiable as δ-$CsPbI_3$. Fig. 1d presents the lattice constants and microstrain of the perovskite thin films. The lattice constants of the perovskite films calculated from Bragg's law, and the introduction of Cs ions leads to a reduction in lattice constants. However, the lattice constants increase upon the introduction of 40 % Cs ions, and this increment is attributed to the reduction of Cs ions in the perovskite lattice following the formation of δ-$CsPbI_3$. Stresses within the perovskite crystal induce microstrain on the perovskite crystal, reflected in the broadening of the diffraction peaks in the perovskite films. In addition to the strain-induced peak broadening, the grain size also contributed to the peak broadening. To distinguish between these two effects, we analyze the diffraction peaks of the perovskite films using the Williamson-Hall plot (Eq. (1)):[29]

$$\beta_{total}cos\theta = \frac{K\lambda}{D} + 4\varepsilon\, sin\theta$$

Where β_{total} is the diffraction peak half-peak width, K is the morphology factor, D is the grain size of perovskite film, and λ is the wavelength of X-ray source (Cu K_α). The slope of the fitted line is indicative of the strain within the perovskite film, while the y-intercept corresponds to the crystallite size of the perovskite film. As illustrated in Fig. S4, the slopes for Cs10Br25, Cs20Br20, Cs30Br15, and Cs40Br10 films are -6.37×10^{-4}, -2.54×10^{-4}, -1.08×10^{-4}, and 1.92×10^{-3},

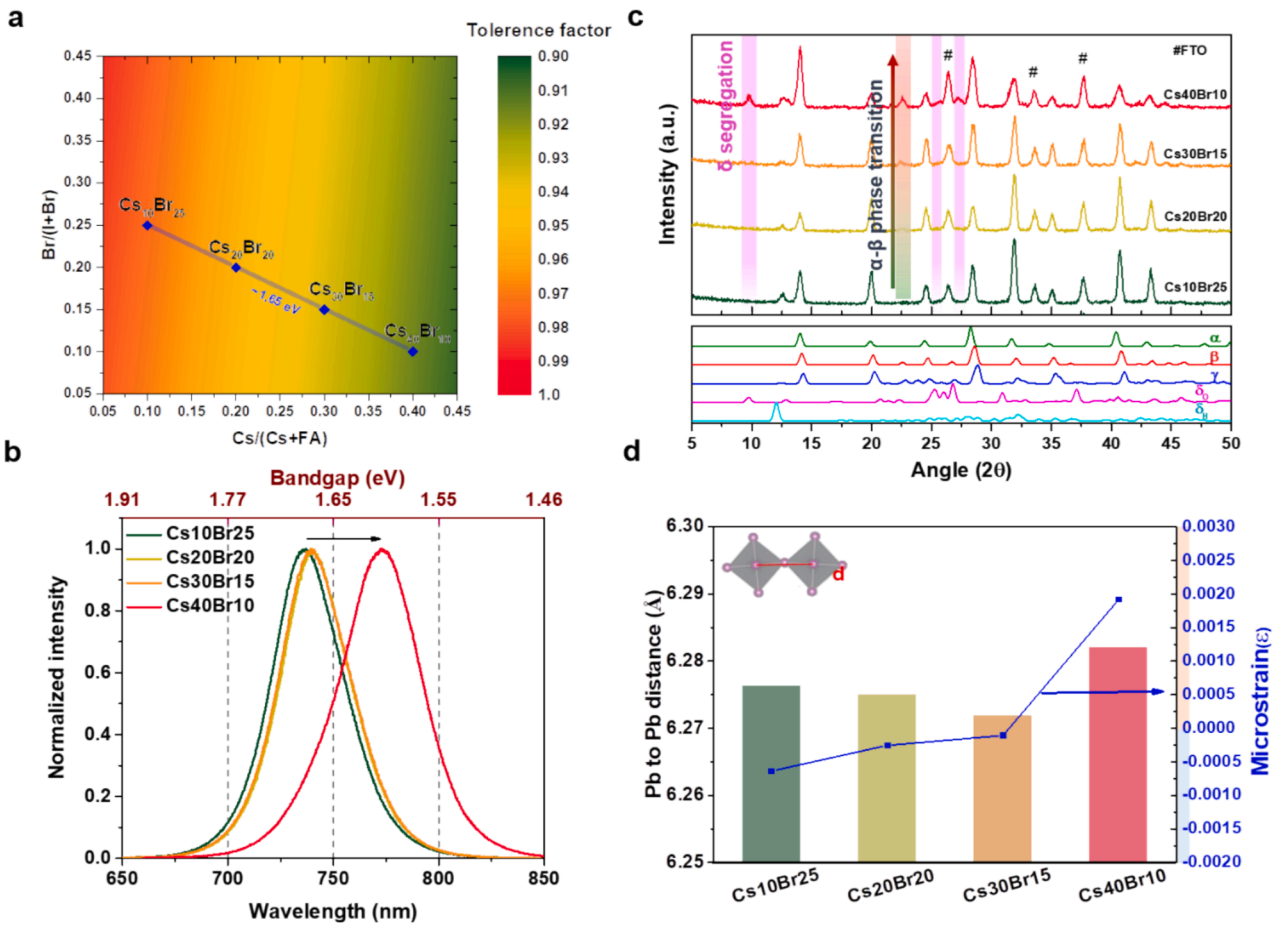

Fig. 1. Characterization of Perovskite films with different composition. (a) Relationship between perovskite composition and tolerance factor. (b) Photo-luminescence profiles. (c) XRD patterns. (# signal relate to the FTO substrate ; reference phase was α-phase as α, β-phase as β, γ-phase as γ, δ_o as orthorhombic-δ-phase and δ_H as hexagonal-δ-phase) (d) Comparison of lattice constant and microstrain.

respectively. It's essential to clarify that the negative values in the Williamson-Hall plot analysis do not imply compressive lattice strains. Instead, they indicate that the microstrain has a negligible effect on the broadening of the diffraction peaks.[30] This result suggests that the diffraction peaks broadening is negligible when Cs ions doping remains below 30 %. However, as Cs ion doping increases to 40 %, the slope becomes positive, signifying the presence of non-negligible microstrain within the perovskite lattice. We illustrate two primary reasons for the phase segregation observed in WBG perovskite films, photo-induced and microstrain-induced phase segregation, as shown in Fig. S5. Photo-induced phase segregation predominantly occurs in perovskite films with high Br ion concentrations under light illumination, which can be mitigated by reducing Br content and increasing Cs content. In contrast, microstrain-induced phase segregation results from lattice microstrain arising from the accumulation of lattice stress because of excessive Cs ion incorporation. The Cs30Br15 composition was selected for further study.

The utilization of perovskite films based on the Cs-FA mixed ion system has garnered extensive attention owing to their remarkable thermal stability and resistance to humidity. However, this system is prone to segregation due to the substantial difference in the solubility of the salts, particularly CsBr. M. I. Saidaminov *et al.* demonstrated that when employing the anti-solvent method to fabricate Cs-FA-based perovskite films, these films exhibited non-uniform regions with an excess of CsBr, particularly in WBG perovskite regions near grain boundaries due to segregation. This phenomenon, in turn, resulted in a reduction of the carrier diffusion length.[31] Therefore, it is very important to enhance the carrier diffusion length in the PSCs fabricated from Cs-FA mixed ion system. Initially, we introduced three solvents, ether, toluene, and ethyl acetate, into the solution of Cs-FA mixed ion perovskite precursor solution, with the results presented in Fig. S6. The results revealed that the addition of ether and toluene did not induce a phase transition, whereas the incorporation of ethyl acetate triggered the formation of the characteristic black perovskite phase. This variance could be attributed to the solubility of the perovskite precursor and the solvent. A. D. Taylor *et al.* emphasized that anti-solvents such as ether and toluene necessitate a prolonged interaction with the perovskite film to effectively remove the host solvent and promote the formation of the crystalline perovskite phase.[32] However, a slow phase transition process could hinder the formation of a uniform and segregation-free perovskite phase. Consequently, ethyl acetate proves to be a more suitable anti-solvent for WBG Cs-FA mixed-ion perovskite systems requiring rapid phase transition. To further explore the phase transition process of perovskite materials, we conducted a titration test on perovskite precursor solutions containing different added cations. Our findings indicate that the addition of rubidium (Rb) ions, methylene diamine (MDA) ions, and guanidine (GA) ions led to the early formation of black perovskite precipitates with minimal titration. This implies that the perovskite can reach oversaturation more swiftly following spin-coating with the anti-solvent, thereby impeding segregation. At an additive content of 5 %, the bandgap of the perovskite film, as determined by the Tauc plot, exhibited negligible change (approximately 0.01 eV) after the introduction of cationic salts (Fig. S7). Therefore, the strategic use of a small quantity of cationic additives serves as a practical approach to modulate the phase transition process of perovskite materials. Additionally, our investigation encompasses the evaluation of

various aspects, including the size, polarity, and valence of the incorporated cations, to gain a deeper understanding of their impact on the structure and photoelectric properties of the perovskite films.

Fig. 2a shows the tolerance factor of perovskite materials based on the different cation sizes. Fig. 2b presents the crystallization behaviors of cation-doped perovskite films using XRD measurements. When doped with GA ions possessing a relatively large ionic radius, these perovskite films manifest one-dimensional precipitation phases, indicating the ineffective doping of GA ions into the perovskite lattice. In contrast, the introduction of Rb ions and MDA ions has a limited impact on the lattice structure of the perovskite phase. Utilizing the Williamson-Hall plot to assess the XRD signals of cation-doped perovskite films (Fig. 2c), we identified a more pronounced microstrain in the MDA-doped perovskite film. This result implies that while MDA ions can be successfully incorporated into the perovskite lattice, the stronger inter-ionic forces arising from their differing valences induce more significant lattice stress and thus a greater microstrain. However, Rb-doped and GA-doped perovskite films exhibit no substantial microstrain. MDA ion is bivalent and easily form more hydrogen bonds to iodine from the perovskite crystal structure.[33] This strong interaction between MDA and the perovskite induces strain within the crystal during the perovskite formation. In contrast, the polarities of Rb and GA are not as pronounced as that of MDA, resulting in the absence of distortion in the XRD patterns of perovskite when doped with Rb or GA. In addition to examining the effect of cation doping on the band alignment of perovskite films, we conducted an analysis of the Fermi level, highest valence band, and lowest conduction band of these films, as illustrated in Fig. 2d and e. The results indicate that the overall energy level shifts downward upon the introduction of smaller Rb ions. In contrast, the introduction of larger GA ions leads to an upward shift in the overall energy level. This phenomenon may be attributed to the tilting angle of the perovskite crystal.

[34,35] The downward shift in energy levels upon the introduction of Rb ions primarily results from the smaller Rb ions entering the perovskite crystal lattice, thereby reducing the B-X-B bond angle and diminishing the hybridization of the B-X orbital domain. It's noteworthy that the MDA-doped perovskite film exhibits a more considerable shift in energy levels compared to the GA-doped perovskite film, likely due to the enhanced mixing of MDA ions into the perovskite lattice in contrast to GA ions. Additionally, the Fermi level shift in the MDA-doped perovskite also signifies N-type doping, possibly due to the variance in MDA ion valence. The device performance of cation-doped WBG PSCs is presented in Table S1. Among the various cation-doped WBG PSCs, the Rb-doped WBG PSCs demonstrate the highest PCE, aligning with the perovskite characterization. Therefore, doping WBG perovskite with Rb ions is the most effective strategy for enhancing phase stability without inducing significant microstrain (Fig. 2f).

We conducted measurements of transient photovoltage (TPV) and transient photocurrent (TPC) to assess carrier lifetime and extraction lifetime in various cation-doped perovskite solar cells. The results, illustrated in Fig. S8, are as follows: In TPV measurements, the carrier lifetimes for pristine, Rb-doped, MDA-doped, and GA-doped perovskite films are 447.78 μs, 597.70 μs, 274.66 μs, and 180.83 μs, respectively. The longest carrier lifetime is observed in Rb-doped perovskite films, suggesting diminished recombination due to defects in these films. Regarding TPC results, the carrier extraction lifetimes for pristine, Rb-doped, MDA-doped, and GA-doped perovskite films are 0.48 μs, 0.47 μs, 0.55 μs, and 0.48 μs, respectively. Significantly, MDA-doped perovskite films exhibit an extended carrier extraction time, potentially attributed to ionized impurity scattering centers generated by increased microstrain stress affecting carrier transport. The perovskite containing microstrain changes the crystal structure, reducing the Gibbs free energy of cubic perovskite through unit cell contraction and cation disorder.

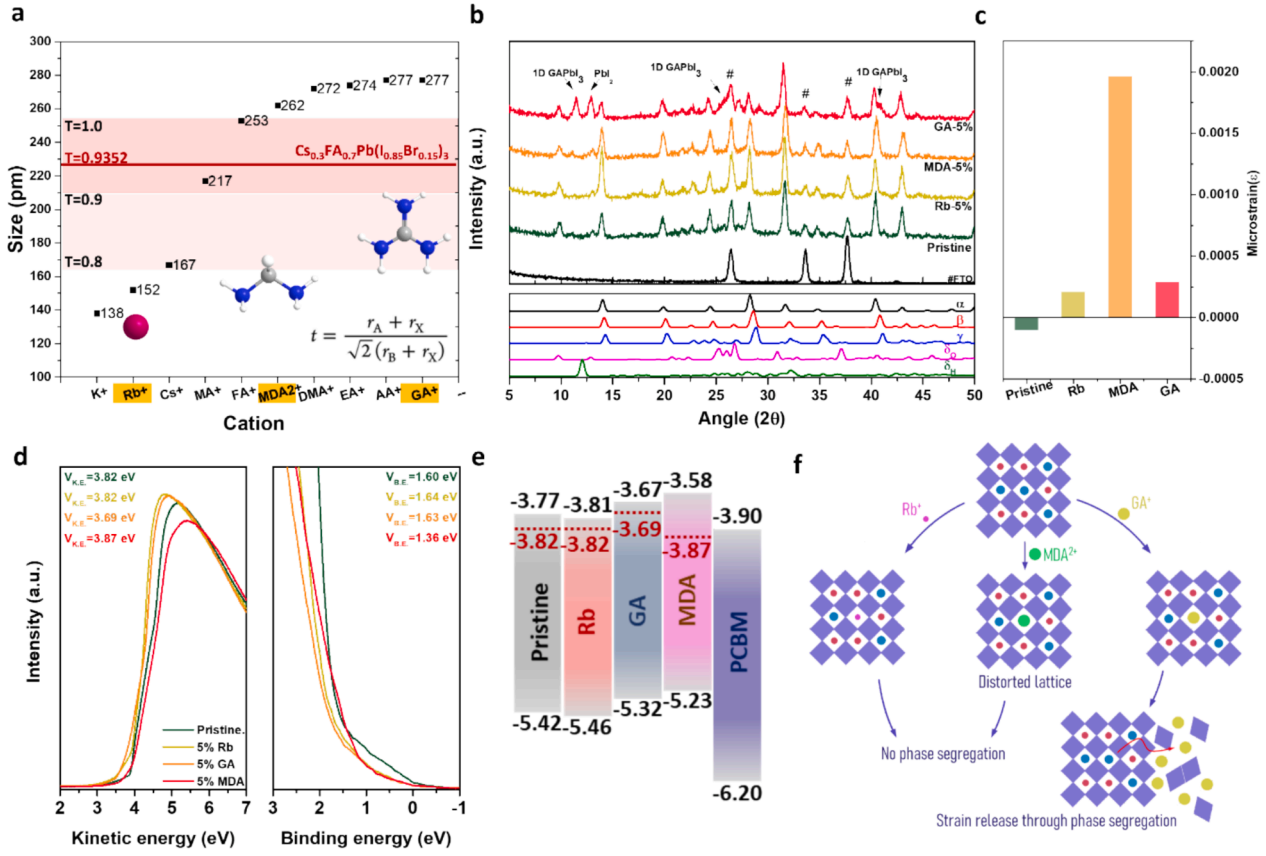

Fig. 2. (a) The ionic size of different cation. (b) XRD patterns, (c) calculated microstrain, (d) UPS spectra, and (e) energy level of perovskite thin films with different A-site dopant. (f) The schematic diagram of how dopants affect to perovskite lattice.

[36] To gain further insights into the carrier lifetime extension mechanism in Rb-doped perovskite films, we explored the effects of different light intensities on V_{oc} and short-circuit current density (J_{sc}) in the devices. As illustrated in Fig. 3a and b, the ideality factors (n_{id}) of pristine and Rb-doped perovskite films are 1.255 and 1.019, respectively. Generally, the n_{id} value close to 1 indicates that a device tends to behave like an ideal diode, where the primary losses are attributed to dark currents in the neutral region or radiative recombination (interband recombination). This result signifies that Rb doping effectively fills deep defects in the perovskite films and reduces charge recombination in the transport process. We also used Drive level capacitance profiling (DLCP) to validate the results observed by the experiment, as shown in Fig. 3c. In addition, we conducted an analysis of the impact of defects on carrier recombination and extraction using electrochemical impedance spectroscopy (EIS). Fig. 3d reveals that the recombination resistances of pristine and Rb-doped perovskite films are 924 Ω and 1060 Ω, respectively, aligning with the n_{id} result. The introduction of an appropriate quantity of Rb ions effectively diminishes the deep trap energy levels within the perovskite films, thereby extending the carrier lifecycle of these films. Moreover, the accumulation of charge generated by the movement of ions in the perovskite films can influence device capacitance under photoexcitation conditions. We utilized photoexcitation-assisted capacitance–voltage (CV) spectroscopy to explore interfacial charge accumulation behavior. As presented in Fig. 3e and f, V_{peak} shifts from a high voltage to a low voltage, with the magnitude of this shift corresponding to the degree of charge accumulation during device operation. V_{peak} denotes the voltage initially injected into the charge carriers, implying that as light intensity increases, charge accumulation neutralizes photo-induced charges, consequently reducing capacitance values. Comparatively, V_{peak} shifts by 75 mV for pristine PSCs and 19 mV for Rb-doped PSCs, demonstrating that the inclusion of Rb ions effectively mitigates interfacial charge accumulation within the perovskite films.

Finally, we assess the photovoltaic performance of pristine and Rb-doped PSCs (Fig. 4a–d). Notably, the average J_{sc} of the devices increases from 20.49 mA/cm^2 to 22.26 mA/cm^2 following the introduction of Rb ions, which proves the role of Rb ions in enhancing carrier extraction in the devices. In addition, the average fill factor (FF) of Rb-doped PSCs rises from 75.13 % (in pristine PSCs) to 79.35 %, which can be attributed to the effective filling of defects in the perovskite film by Rb ions. Consequently, the average PCE of the devices improved from 17.75 % to 20.54 %. The highest PCE achieved in Rb-doped PSCs reaches 22.11 %, demonstrating competitive PCE among MA-free inverted-type WBG PSCs (1.65 eV) reported to date (refer to Fig. 4e and Table S2). This suggests that Rb-doped PSCs exhibit superior reproducibility. Fig. 4f presents the forward and reverse J-V curves of the Rb-doped device, demonstrating no hysteresis in the Rb-doped WBG PSCs. As shown in Fig. 4g and h, our results closely approach the Shockley-Queisser limit, in contrast to the data reported in the literature.[37] To further demonstrate the phase stability of MA-free WBG PSC, we have added the light soaking test comparing WBG PSCs with MA and without MA, as shown in Fig. S9. The MA-containing WBG PSC was prepared with a composition of 10 mol% MA-doped WBG. During the light soaking test, the intensity of light is conducted at 100 mW/cm^2. The T_{80} lifetime for the MA-containing WBG PSCs was below 10 h. Then, the MA-free WBG PSCs was maintained 84 % of their initial PCE over 186 h. It indicated that the MA-free WBG PSCs exhibit better light-soaking stability of, likely due to the presence of volatile MA molecules in the MA-containing WBG. Then, we extend the PL irradiation time for the Rb-doped MA-free perovskite film, as shown in Fig. S10. The PL intensity of the Rb-doped MA-free perovskite film remained consistent for over 30 min without any peak shifts, indicating significant phase stability of the MA-free perovskite film attributable to Rb doping in the perovskite crystal structure. Moreover, we extended our investigations to the fabrication of Rb-doped semi-transparent PSCs (ST-PSCs). The transmittance of the Rb-doped ST-PSCs is illustrated in Fig. S11. We subsequently mechanically stacked these ST-PSCs onto silicon bottom cells to fabricate 4T tandem solar cells. These fabrications followed procedures detailed in

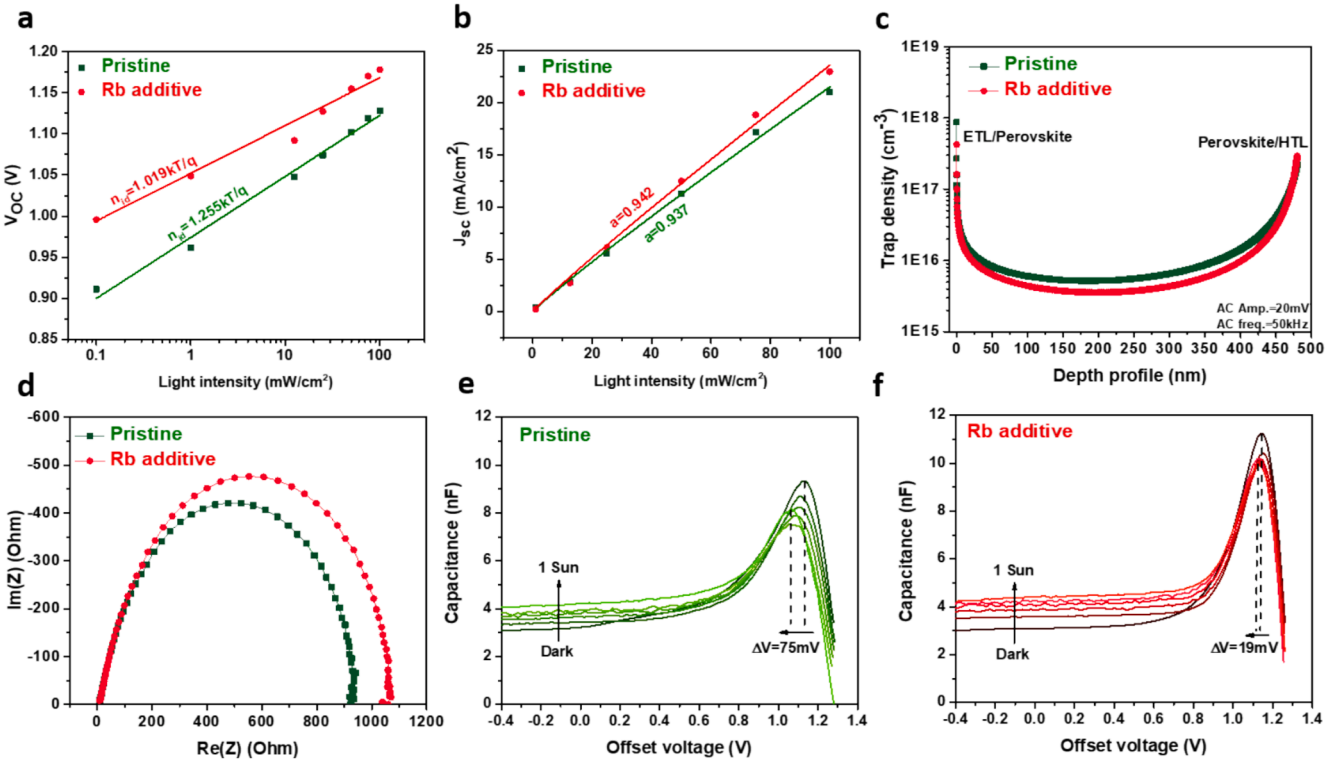

Fig. 3. The analysis of carrier dynamics of devices without and with Rb-doped: (a-b) the J_{sc} and V_{oc} dependent on light intensity. (c) Drive level capacitance profiling, (d) impedance spectroscopy, and (e-f) photoexcitation-assisted capacitance–voltage spectroscopy.

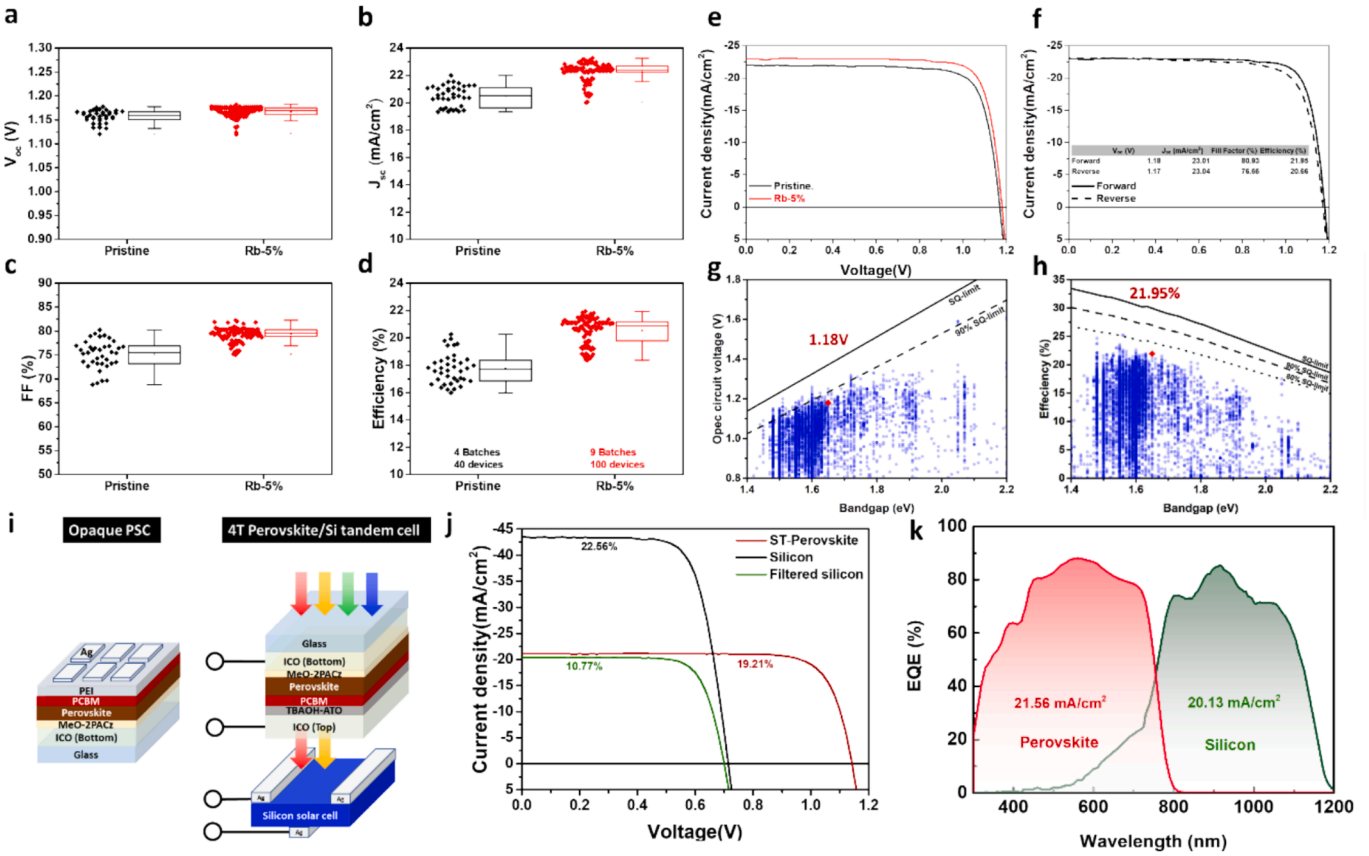

Fig. 4. Performance distribution of without and with Rb-doped devices: (a) V_{oc}, (b) Jsc, (c) fill factor (d) PCE (e) J-V curves (f) The forward and reverse J-V curves of Rb-doped device (hysteresis effect) (g-h) The reported photovoltaic parameters of perovskite solar cells.[37] (i) Device structure of PSC and 4T tandem cells. The (j) J-V curves (k) EQE data of 4-T perovskite/silicon tandem solar cells.

our previous study.[38] The device structure of PSC and 4 T tandem cells were shown in Fig. 4i. Fig. 4j presents the J-V curves of the 4T tandem solar cells, while Table 1 provides an overview of relevant photovoltaic characteristics. The individual HJT c-Si solar cell exhibits a PCE of 22.56 %, featuring a V_{oc} of 0.71 V, J_{sc} of 43.59 mA/cm^2, and an FF of 72.48 %. Notably, the J_{sc} of the HJT c-Si solar cells, when filtered by ST-PSCs, reaches 20.44 mA/cm^2. Calculations show a remarkable J_{sc} retention rate of 46.9 %, marking a substantial increase compared to our previous results (39.5 %). This boost in J_{sc} retention can be attributed to the high visible light transmittance of the wide bandgap perovskite layer. Fig. 4k illustrates external quantum efficiency (EQE) spectra for standalone and filtered c-Si solar cells, with integrated J_{sc} values from EQE spectra aligning with J_{sc} data obtained from J-V curves. As a result, the PCE for the filtered c-Si solar cell and the 4T tandem solar cell reaches 10.77 % and 29.98 %, respectively (Table 1). Furthermore, the absolute PCE of the tandem solar cells is significantly determined by the initial PCE of the stand-alone Si-based solar cell. Considering the difference in initial PCE of the c-Si solar cells, therefore, the PCE gain obtained after tandem is a more objective and important index compared to the final PCE of the tandem solar cells. We have summarized the current progress of the 4T tandem solar cells, and calculated the PCE gain of the 4T tandem solar cells relative to the initial PCE of c-Si solar cells, detailed in Table S3. Notably, our approach attains an impressive PCE gain of 32.89 %. This highlights the excellent performance of our results and methodology in the field of 4T tandem solar cells.

Table 1
Photovoltaics characteristics of pristine, Rb-doped perovskite solar cells, and perovskite/ silicon tandem solar cells.

Sample	V_{oc}(V)	J_{sc}(mA/cm^2)	FF(%)	PCE(%)
Pristine	1.16 ± 0.01 (1.17)	20.49 ± 0.75 (22.01)	75.13 ± 2.89 (78.87)	17.75 ± 1.11 (20.27)
Rb-doped	1.17 ± 0.01 (1.18)	22.26 ± 0.71 (23.07)	79.35 ± 1.48 (81.50)	20.54 ± 0.97 (22.11)
HJT	0.72 ± 0.00 (0.71)	42.75 ± 0.98 (43.59)	71.45 ± 1.24 (72.48)	21.88 ± 0.61 (22.56)
ST-perovskite	1.13 ± 0.01 (1.14)	20.38 ± 0.54 (21.12)	79.26 ± 0.57 (79.74)	18.30 ± 0.67 (19.21)
Filter-silicon	0.70 ± 0.00 (0.70)	20.26 ± 0.43 (20.44)	74.56 ± 1.98 (75.27)	10.52 ± 0.16 (10.77)
4T solar cell				27.96 (29.98)

3. Conclusions

We present a comprehensive set of optimization procedures designed to enhance the performance of perovskite compositions with different bandgaps. Furthermore, we offer effective methods for identifying and rectifying the causes of instability in MA-free WBG perovskites. In Cs-FA perovskite systems, the bandgap can be systematically augmented by elevating the Cs-to-Br ratio. Our research highlights the enhanced stability exhibited by the pure β-phase tetragonal system. We further introduced cationic salts to fine-tune the photovoltaic performance of the mixed cation perovskite system containing Cs and FA. Our investigations demonstrated that the Rb-doped perovskite layer not only expedited the phase transition but also optimized the energy level alignment with the ETL. In comparison to undoped PSCs, our modified devices exhibited a noteworthy increase in average efficiency, rising from 17.75 % to 20.54 %, with the highest efficiency reaching 22.11 %. Lastly, the semi-transparent perovskite solar cells produced by our system attained a peak efficiency of 19.21 %. When combined with HJT

silicon solar cells, the 4T tandem solar cell developed in this study obtained an overall PCE of 29.98 % and achieved an impressive PCE gain of 32.84 %.

CRediT authorship contribution statement

Yu-Ching Huang: Writing – review & editing, Supervision, Resources, Project administration, Funding acquisition, Conceptualization. **Sheng-Wen Huang:** Writing – original draft, Validation, Methodology, Investigation, Formal analysis, Data curation. **Chia-Feng Li:** Validation, Methodology, Investigation, Formal analysis, Data curation. **Shih-Han Huang:** Writing – original draft, Validation, Formal analysis, Data curation. **Feng-Yu Tsai:** Supervision. **Wei-Fang Su:** Supervision, Conceptualization.

Declaration of competing interest

The authors declare that they have no known competing financial interests or personal relationships that could have appeared to influence the work reported in this paper.

Acknowledgements

Financial support provided by the National Science and Technology Council of Taiwan (Grant Nos. NSTC 112-2628-E-131-001-MY4, NSTC 111-2221-E-182-040-MY3 and NSTC 113-2622-E-131-006-) and Chang Gung University (URRPD2N0011) are highly appreciated.

Appendix A. Supplementary data

Supplementary data to this article can be found online at https://doi.org/10.1016/j.cej.2024.158272.

Data availability

Data will be made available on request.

References

[1] W. Shockley H. Queisser Detailed balance limit of efficiency of p–n junction solar cells Renewable Energy, Routledge 2018 pp. Vol2_35-Vol2_54.
[2] N.V. Yastrebova, High-efficiency multi-junction solar cells, in: Current Status and Future Potential, Centre for Research in Photonics, University of Ottawa, 2007, p. 17.
[3] X. Chen, Z. Jia, Z. Chen, T. Jiang, L. Bai, F. Tao, J. Chen, X. Chen, T. Liu, X. Xu, C. Yang, W. Shen, W.E.I. Sha, H. Zhu, Y. Yang, Efficient and Reproducible Monolithic Perovskite/Organic Tandem Solar Cells with Low-Loss Interconnecting Layers, Joule 4 (7) (2020) 1594–1606, https://doi.org/10.1016/j.joule.2020.06.006.
[4] Y. Cheng, L. Ding, Perovskite/Si tandem solar cells: Fundamentals, advances, challenges, and novel applications, SusMat 1 (3) (2021) 324–344, https://doi.org/10.1002/sus2.25.
[5] M. Jošt, E. Köhnen, A. Al-Ashouri, T. Bertram, Š. Tomšič, A. Magomedov, E. Kasparavicius, T. Kodalle, B. Lipovšek, V. Getautis, R. Schlatmann, C.A. Kaufmann, S. Albrecht, M. Topič, Perovskite/CIGS Tandem Solar Cells: From Certified 24.2% toward 30% and Beyond, ACS Energy Letters 7(4) (2022) 1298-1307. https://doi.org/10.1021/acsenergylett.2c00274.
[6] R. Lin, Y. Wang, Q. Lu, B. Tang, J. Li, H. Gao, Y. Gao, H. Li, C. Ding, J. Wen, P. Wu, C. Liu, S. Zhao, K. Xiao, Z. Liu, C. Ma, Y. Deng, L. Li, F. Fan, H. Tan, All-perovskite tandem solar cells with 3D/3D bilayer perovskite heterojunction, Nature 620 (7976) (2023) 994–1000, https://doi.org/10.1038/s41586-023-06278-z.
[7] M.A. Mahmud, J. Zheng, S. Tang, C. Liao, G. Wang, J. Bing, T.L. Leung, A.D. Bui, H. Chen, J. Yi, S.P. Bremner, H.T. Nguyen, A.W.Y. Ho-Baillie, Water-Free, Conductive Hole Transport Layer for Reproducible Perovskite–perovskite Tandems with Record Fill Factor, ACS Energy Letters 8 (1) (2023) 21–30, https://doi.org/10.1021/acsenergylett.2c02164.
[8] X. Wang, D. Zhang, B. Liu, X. Wu, X. Jiang, S. Zhang, Y. Wang, D. Gao, L. Wang, H. Wang, Z. Huang, X. Xie, T. Chen, Z. Xiao, Q. He, S. Xiao, Z. Zhu, S. Yang, Highly Efficient Perovskite/Organic Tandem Solar Cells Enabled by Mixed-Cation Surface Modulation, Adv. Mater. 35 (49) (2023) 2305946, https://doi.org/10.1002/adma.202305946.
[9] Y.-M. Xie, Q. Xue, Q. Yao, S. Xie, T. Niu, H.-L. Yip, Monolithic perovskite/organic tandem solar cells: Developments, prospects, and challenges, Nano Select 2 (7) (2021) 1266–1276, https://doi.org/10.1002/nano.202000287.
[10] Y. Li, Y. Lu, X. Huo, D. Wei, J. Meng, J. Dong, B. Qiao, S. Zhao, Z. Xu, D. Song, Bandgap tuning strategy by cations and halide ions of lead halide perovskites learned from machine learning, RSC Adv. 11 (26) (2021) 15688–15694, https://doi.org/10.1039/D1RA03117A.
[11] M. Saliba, T. Matsui, K. Domanski, J.-Y. Seo, A. Ummadisingu, S.M. Zakeeruddin, J.-P. Correa-Baena, W.R. Tress, A. Abate, A. Hagfeldt, M. Grätzel, Incorporation of rubidium cations into perovskite solar cells improves photovoltaic performance, Science 354 (6309) (2016) 206–209, https://doi.org/10.1126/science.aah5557.
[12] Y. Zheng, X. Wu, J. Liang, Z. Zhang, J. Jiang, J. Wang, Y. Huang, C. Tian, L. Wang, Z. Chen, C.-C. Chen, Downward Homogenized Crystallization for Inverted Wide-Bandgap Mixed-Halide Perovskite Solar Cells with 21% Efficiency and Suppressed Photo-Induced Halide Segregation, Adv. Funct. Mater. 32 (29) (2022) 2200431, https://doi.org/10.1002/adfm.202200431.
[13] B. Chen, Z. Yu, K. Liu, X. Zheng, Y. Liu, J. Shi, D. Spronk, P.N. Rudd, Z. Holman, J. Huang, Grain Engineering for Perovskite/Silicon Monolithic Tandem Solar Cells with Efficiency of 25.4%, Joule 3(1) (2019) 177-190. https://doi.org/https://doi.org/10.1016/j.joule.2018.10.003.
[14] J. Sala, M. Heydarian, S. Lammar, Y. Abdulraheem, T. Aernouts, A. Hadipour, J. Poortmans, Compositional Investigation for Bandgap Engineering of Wide Bandgap Triple Cation Perovskite, ACS Appl. Energy Mater. 4 (7) (2021) 6377–6384, https://doi.org/10.1021/acsaem.1c00810.
[15] D. Kim, H.J. Jung, I.J. Park, B.W. Larson, S.P. Dunfield, C. Xiao, J. Kim, J. Tong, P. Boonmongkolras, S.G. Ji, F. Zhang, S.R. Pae, M. Kim, S.B. Kang, V. Dravid, J. J. Berry, J.Y. Kim, K. Zhu, D.H. Kim, B. Shin, Efficient, stable silicon tandem cells enabled by anion-engineered wide-bandgap perovskites, Science 368 (6487) (2020) 155–160, https://doi.org/10.1126/science.aba3433.
[16] M.I. Saidaminov, J. Kim, A. Jain, R. Quintero-Bermudez, H. Tan, G. Long, F. Tan, A. Johnston, Y. Zhao, O. Voznyy, E.H. Sargent, Suppression of atomic vacancies via incorporation of isovalent small ions to increase the stability of halide perovskite solar cells in ambient air, Nat. Energy 3 (8) (2018) 648–654, https://doi.org/10.1038/s41560-018-0192-2.
[17] M. Kim, G.-H. Kim, T.K. Lee, I.W. Choi, H.W. Choi, Y. Jo, Y.J. Yoon, J.W. Kim, J. Lee, D. Huh, H. Lee, S.K. Kwak, J.Y. Kim, D.S. Kim, Methylammonium Chloride Induces Intermediate Phase Stabilization for Efficient Perovskite Solar Cells, Joule 3 (9) (2019) 2179–2192, https://doi.org/10.1016/j.joule.2019.06.014.
[18] B.-W. Park, H.W. Kwon, Y. Lee, D.Y. Lee, M.G. Kim, G. Kim, K.-J. Kim, Y.K. Kim, J. Im, T.J. Shin, S.I. Seok, Stabilization of formamidinium lead triiodide α-phase with isopropylammonium chloride for perovskite solar cells, Nat. Energy 6 (4) (2021) 419–428, https://doi.org/10.1038/s41560-021-00802-z.
[19] L. Yan, H. Huang, P. Cui, S. Du, Z. Lan, Y. Yang, S. Qu, X. Wang, Q. Zhang, B. Liu, X. Yue, X. Zhao, Y. Li, H. Li, J. Ji, M. Li, Fabrication of perovskite solar cells in ambient air by blocking perovskite hydration with guanabenz acetate salt, Nat. Energy 8 (10) (2023) 1158–1167, https://doi.org/10.1038/s41560-023-01358-w.
[20] T. Pan, W. Zhou, Q. Wei, Z. Peng, H. Wang, X. Jiang, Z. Zang, H. Li, D. Yu, Q. Zhou, M. Pan, W. Zhou, Z. Ning, Surface-Energy-Regulated Growth of α-Phase $Cs_{0.03}FA_{0.97}PbI_3$ for Highly Efficient and Stable Inverted Perovskite Solar Cells, Adv. Mater. 35 (15) (2023) 2208522, https://doi.org/10.1002/adma.202208522.
[21] H. Zhou, L. Yang, Y. Duan, M. Wu, Y. Li, D. Xu, H. Zou, J. Wang, S. Yang, Z. Liu, 24.96%-Efficiency $FACsPbI_3$ Perovskite Solar Cells Enabled by an Asymmetric 1,3-Thiazole-2,4-Diammonium, Adv. Energy Mater. 13 (15) (2023) 2204372, https://doi.org/10.1002/aenm.202204372.
[22] R. Chen, J. Wang, Z. Liu, F. Ren, S. Liu, J. Zhou, H. Wang, X. Meng, Z. Zhang, X. Guan, W. Liang, P.A. Troshin, Y. Qi, L. Han, W. Chen, Reduction of bulk and surface defects in inverted methylammonium- and bromide-free formamidinium perovskite solar cells, Nat. Energy 8 (8) (2023) 839–849, https://doi.org/10.1038/s41560-023-01288-7.
[23] D. Liu, D. Luo, A.N. Iqbal, K.W.P. Orr, T.A.S. Doherty, Z.-H. Lu, S.D. Stranks, W. Zhang, Strain analysis and engineering in halide perovskite photovoltaics, Nat. Mater. 20 (10) (2021) 1337–1346, https://doi.org/10.1038/s41563-021-01097-x.
[24] D.-J. Xue, Y. Hou, S.-C. Liu, M. Wei, B. Chen, Z. Huang, Z. Li, B. Sun, A.H. Proppe, Y. Dong, M.I. Saidaminov, S.O. Kelley, J.-S. Hu, E.H. Sargent, Regulating strain in perovskite thin films through charge-transport layers, Nat. Commun. 11 (1) (2020) 1514, https://doi.org/10.1038/s41467-020-15338-1.
[25] X. Zhuang, D. Zhou, S. Liu, Z. Shi, R. Sun, J. Liang, Y. Jia, S. Bian, Z. Liu, H. Song, Trivalent Europium-Doped CsCl Quantum Dots for MA-Free Perovskite Solar Cells with Inherent Bandgap through Lattice Strain Compensation, Adv. Mater. 35 (40) (2023) 2302393, https://doi.org/10.1002/adma.202302393.
[26] C.G. Bischak, C.L. Hetherington, H. Wu, S. Aloni, D.F. Ogletree, D.T. Limmer, N. S. Ginsberg, Origin of Reversible Photoinduced Phase Separation in Hybrid Perovskites, Nano Lett. 17 (2) (2017) 1028–1033, https://doi.org/10.1021/acs.nanolett.6b04453.
[27] M.C. Brennan, S. Draguta, P.V. Kamat, M. Kuno, Light-Induced Anion Phase Segregation in Mixed Halide Perovskites, ACS Energy Lett. 3 (1) (2018) 204–213, https://doi.org/10.1021/acsenergylett.7b01151.
[28] S.K. Gautam, M. Kim, D.R. Miquita, J.-E. Bourée, B. Geffroy, O. Plantevin, Reversible Photoinduced Phase Segregation and Origin of Long Carrier Lifetime in Mixed-Halide Perovskite Films, Adv. Funct. Mater. 30 (28) (2020) 2002622, https://doi.org/10.1002/adfm.202002622.
[29] G.K. Williamson, W.H. Hall, X-ray line broadening from filed aluminium and wolfram L'elargissement des raies de rayons x obtenues des limailles d'aluminium et de tungsteneDie verbreiterung der roentgeninterferenzlinien von aluminium- und wolframspaenen, Acta Metall. 1 (1) (1953) 22–31, https://doi.org/10.1016/0001-6160(53)90006-6.
[30] J. Langford, R. Cernik, D. Louer, The breadth and shape of instrumental line profiles in high-resolution powder diffraction, J. Appl. Cryst. 24 (5) (1991) 913–919.

[31] M.I. Saidaminov, K. Williams, M. Wei, A. Johnston, R. Quintero-Bermudez, M. Vafaie, J.M. Pina, A.H. Proppe, Y. Hou, G. Walters, S.O. Kelley, W.A. Tisdale, E. H. Sargent, Multi-cation perovskites prevent carrier reflection from grain surfaces, Nat. Mater. 19 (4) (2020) 412–418, https://doi.org/10.1038/s41563-019-0602-2.

[32] A.D. Taylor, Q. Sun, K.P. Goetz, Q. An, T. Schramm, Y. Hofstetter, M. Litterst, F. Paulus, Y. Vaynzof, A general approach to high-efficiency perovskite solar cells by any antisolvent, Nat. Commun. 12 (1) (2021) 1878, https://doi.org/10.1038/s41467-021-22049-8.

[33] G. Kim, H. Min, K.S. Lee, D.Y. Lee, S.M. Yoon, S.I. Seok, Impact of strain relaxation on performance of α-formamidinium lead iodide perovskite solar cells, Science 370 (6512) (2020) 108–112, https://doi.org/10.1126/science.abc4417.

[34] R. Prasanna, A. Gold-Parker, T. Leijtens, B. Conings, A. Babayigit, H.-G. Boyen, M. F. Toney, M.D. McGehee, Band Gap Tuning via Lattice Contraction and Octahedral Tilting in Perovskite Materials for Photovoltaics, J. Am. Chem. Soc. 139 (32) (2017) 11117–11124, https://doi.org/10.1021/jacs.7b04981.

[35] S. Tao, I. Schmidt, G. Brocks, J. Jiang, I. Tranca, K. Meerholz, S. Olthof, Absolute energy level positions in tin- and lead-based halide perovskites, Nat. Commun. 10 (1) (2019) 2560, https://doi.org/10.1038/s41467-019-10468-7.

[36] L.-Q. Xie, L. Chen, Z.-A. Nan, H.-X. Lin, T. Wang, D.-P. Zhan, J.-W. Yan, B.-W. Mao, Z.-Q. Tian, Understanding the Cubic Phase Stabilization and Crystallization Kinetics in Mixed Cations and Halides Perovskite Single Crystals, J. Am. Chem. Soc. 139 (9) (2017) 3320–3323, https://doi.org/10.1021/jacs.6b12432.

[37] T.J. Jacobsson, A. Hultqvist, A. García-Fernández, A. Anand, A. Al-Ashouri, A. Hagfeldt, A. Crovetto, A. Abate, A.G. Ricciardulli, A. Vijayan, A. Kulkarni, A.Y. Anderson, B.P. Darwich, B. Yang, B.L. Coles, C.A.R. Perini, C. Rehermann, D. Ramirez, D. Fairen-Jimenez, D. Di Girolamo, D. Jia, E. Avila, E.J. Juarez-Perez, F. Baumann, F. Mathies, G.S.A. González, G. Boschloo, G. Nasti, G. Paramasivam, G. Martínez-Denegri, H. Näsström, H. Michaels, H. Köbler, H. Wu, I. Benesperi, M.I. Dar, I. Bayrak Pehlivan, I.E. Gould, J.N. Vagott, J. Dagar, J. Kettle, J. Yang, J. Li, J. A. Smith, J. Pascual, J.J. Jerónimo-Rendón, J.F. Montoya, J.-P. Correa-Baena, J. Qiu, J. Wang, K. Sveinbjörnsson, K. Hirselandt, K. Dey, K. Frohna, L. Mathies, L.A. Castriotta, M.H. Aldamasy, M. Vasquez-Montoya, M.A. Ruiz-Preciado, M.A. Flatken, M.V. Khenkin, M. Grischek, M. Kedia, M. Saliba, M. Anaya, M. Veldhoen, N. Arora, O. Shargaieva, O. Maus, O.S. Game, O. Yudilevich, P. Fassl, Q. Zhou, R. Betancur, R. Munir, R. Patidar, S.D. Stranks, S. Alam, S. Kar, T. Unold, T. Abzieher, T. Edvinsson, T.W. David, U.W. Paetzold, W. Zia, W. Fu, W. Zuo, V.R.F. Schröder, W. Tress, X. Zhang, Y.-H. Chiang, Z. Iqbal, Z. Xie, E. Unger, An open-access database and analysis tool for perovskite solar cells based on the FAIR data principles, Nature Energy 7(1) (2022) 107-115. https://doi.org/10.1038/s41560-021-00941-3.

[38] P.-H. Lee, T.-T. Wu, K.-Y. Tian, C.-F. Li, C.-H. Hou, J.-J. Shyue, C.-F. Lu, Y.-C. Huang, W.-F. Su, Work-Function-Tunable Electron Transport Layer of Molecule-Capped Metal Oxide for a High-Efficiency and Stable p–i–n Perovskite Solar Cell, ACS Appl. Mater. Interfaces 12 (41) (2020) 45936–45949, https://doi.org/10.1021/acsami.0c10717.